

RESEARCH PAPER



Cp1/cathepsin L is required for autolysosomal clearance in *Drosophila*

Tianqi Xu^a, Shannon Nicolson^a, Jarrod J. Sandow^{b,c}, Sonia Dayan^a, Xin Jiang^b, Jantina A. Manning^b, Andrew I. Webb^{b,c}, Sharad Kumar^a, and Donna Denton^a

^aCentre for Cancer Biology, University of South Australia and SA Pathology, Adelaide, Australia; ^bAdvanced Technology and Biology, The Walter & Eliza Hall Institute of Medical Research, Parkville, Australia; ^cDepartment of Medical Biology, University of Melbourne, Parkville, Australia

ABSTRACT

Macroautophagy/autophagy is a highly conserved lysosomal degradative pathway important for maintaining cellular homeostasis. Much of our current knowledge of autophagy is focused on the initiation steps in this process. Recently, an understanding of later steps, particularly lysosomal fusion leading to autolysosome formation and the subsequent role of lysosomal enzymes in degradation and recycling, is becoming evident. Autophagy can function in both cell survival and cell death, however, the mechanisms that distinguish adaptive/survival autophagy from autophagy-dependent cell death remain to be established. Here, using proteomic analysis of *Drosophila* larval midguts during degradation, we identify a group of proteins with peptidase activity, suggesting a role in autophagy-dependent cell death. We show that *Cp1/cathepsin L*-deficient larval midgut cells accumulate aberrant autophagic vesicles due to a block in autophagic flux, yet later stages of midgut degradation are not compromised. The accumulation of large aberrant autolysosomes in the absence of *Cp1* appears to be the consequence of decreased degradative capacity as they contain undigested cytoplasmic material, rather than a defect in autophagosome-lysosome fusion. Finally, we find that other cathepsins may also contribute to proper autolysosomal degradation in *Drosophila* larval midgut cells. Our findings provide evidence that cathepsins play an essential role in the autolysosome to maintain basal autophagy flux by balancing autophagosome production and turnover.

Abbreviations: 26-29-p: 26-29kD-proteinase; ADCD: autophagy-dependent cell death; Atg8a: Autophagy-related protein 8a; *Cp1/cathepsin L*: Cysteine proteinase-1; CtsB: Cathepsin B; *cathD*: cathepsin D; CtsF: Cathepsin F; GFP: green fluorescent protein; LAMP1: lysosomal-associated membrane protein 1; Mitf: microphthalmia associated transcription factor; PCA: principal component analysis; RNAi: RNA interference; RPF: relative to puparium formation

ARTICLE HISTORY

Received 3 January 2020
Revised 29 September 2020
Accepted 6 October 2020

KEYWORDS

Autophagy; cell death;
Drosophila; lysosome;
midgut; proteome

Introduction

Cell death is essential for ensuring proper animal development and homeostasis, as well as safeguarding against disease [1–3]. The predominant cell death modalities that occur during development include apoptosis, necroptosis and autophagy-dependent cell death (ADCD) [4]. Macroautophagy (hereafter referred to as autophagy) is the evolutionarily conserved process by which cytoplasmic contents are sequestered into double-membrane autophagosomes and transported to the lysosome for degradation. In seemingly contradictory functions, autophagy is well established as a cell survival process, but can also mediate cell death [5]. Although our understanding of ADCD has recently increased, how autophagy promotes cell death and what distinguishes this from its cell survival mode remains poorly understood. An established model system to study ADCD *in vivo* is the degradation of the *Drosophila* larval midgut.

Regulated cell death of the *Drosophila* larval midgut is triggered in response to a developmentally timed release of the steroid hormone ecdysone during the larval-pupal transition [6,7]. Midgut degradation is dependent upon autophagy,

but not apoptosis as it occurs normally in the absence of the apoptotic machinery yet is blocked by inhibition of autophagy [8,9]. However, only a subset of the multi-subunit complexes that mediate autophagy during cell survival are essential for ADCD [10]. This suggests that novel yet to be identified components are required for autophagy during cell death. In addition, the mechanisms by which autophagy specifically results in the demise of the cell remains to be elucidated.

Lysosomes are degradative organelles with an acidic pH that contain proteolytic enzymes, including cathepsins. The mammalian cathepsin family consists of aspartic (CTSD [cathepsin D] and CTSE [cathepsin E]), cysteine (including CTSB [cathepsin B], CTSC [cathepsin C], CTSH [cathepsin H], CTSK [cathepsin K], and CTSL [cathepsin L]), and serine (CTSA [cathepsin A] and CTSG [cathepsin G]) proteases [11]. Cathepsins have important functions in the immune response, processing and activation of substrates, apoptosis, autophagy, and other processes [11]. Regulating their activity is important, as dysregulation disrupts cellular homeostasis and contributes to several diseases including cancer and neurodegeneration [12].

The progression and resolution of autophagy are dependent on lysosome function, as autophagic flux requires the fusion of the autophagosome with the lysosome, where the contents are degraded and lysosomes are reformed from the autolysosomes [13]. However, the requirement for lysosomal degradation in ADCD remains to be established. Current evidence suggests that the lysosome may contribute to cell death due to autophagy in apoptotic-deficient *bax; bak1* double-knockout mouse embryonic fibroblasts. Starvation-induced autophagic cell death is restored in *bax; bak1* double-knockout mouse embryonic fibroblasts by targeting BAX to the lysosome or by increasing lysosomal membrane permeability [14]. In addition, *Drosophila* larval midgut cells that are deficient for the dpp/BMP/TGF- β (decapentaplegic) signaling components, *Mad* and *tkv*, are rapidly degraded with markers of autophagy and lysosomal activity [15]. This suggests that the bulk degradation of cellular components, such as by the lysosomal enzymes, may result in the demise of the cell. A critical outstanding question to be addressed is how the lysosome contributes to ADCD.

To determine the mechanisms of ADCD, we undertook a proteomic analysis to identify changes in protein abundance during midgut degradation as we predicted that protein abundance might be dynamic during developmental cell death. This analysis identified over 3,000 proteins, including proteins known to have roles in larval midgut cell death. From this, we used genetic approaches to analyze the most significantly changed components in the dataset for a role in midgut degradation. Here, we showed that cathepsins, especially Cp1, are required to properly maintain autophagy flux in the midgut yet, surprisingly, are not required for midgut degradation.

Results

Global quantitative analysis of protein expression in dying *Drosophila* larval midguts

The degradation of the larval midgut during *Drosophila* development is a dynamic process that is initiated by an increase in the titer of ecdysone at -4 h relative to puparium formation (RPF) [6,7]. This results in a reduction of midgut size over time that requires autophagy but not the apoptosis machinery [8,10,16]. To understand how this tissue dies by ADCD, changes in protein abundance during midgut degradation were profiled by analyzing the midgut proteome. Proteins were isolated from midguts at three time points during degradation corresponding to the onset at -4 h RPF, at 0 h RPF and later at +2 h RPF (Figure 1A). The biological replicates from each of these differentially staged midguts were then subjected to quantitation by label-free liquid chromatography-tandem mass spectrometry (LC-MS/MS). A principal component analysis (PCA) using the log₂ intensity values of all peptides detected in the -4, 0 and +2 h RPF midgut samples was performed to examine the variability between the replicates for each sample (Figure 1B; S1A and S1B; as described in Materials and Methods).

In total, 3,713 proteins from 27,427 unique peptides were identified across the course of midgut degradation, with 3,059

proteins identified from at least two unique peptides. The majority of proteins (3,423, 92.2%) were common to all stages of midgut degradation, whereas other proteins were uniquely identified in two stages of midgut cell death or a single stage (Figure 1C). In -4 and 0 h RPF midguts, 83 (2.2%) proteins were uniquely identified while 93 (2.5%) and 31 (0.8%) proteins were common to midguts at 0 and +2 h RPF, and -4 and +2 h RPF, respectively (Figure 1C). This was consistent with the results of the PCA where the -4 and +2 h RPF samples were more separated than the 0 and +2 samples on PC1 (Figure 1B). Proteins were also uniquely identified in each developmental stage including 52 (1.4%) proteins in -4 h RPF midguts, and 9 (0.2%) and 22 (0.6%) in 0 h RPF and +2 h RPF midguts respectively (Figure 1C).

This quantitative proteomic analysis identified several proteins known to be required for autophagy-dependent midgut cell death (Table 1). These proteins included components of the core autophagic machinery, negative upstream regulators of autophagy including the PI3K-Tor pathway, proteins required for ecdysone-mediated signaling, ubiquitination-associated proteins, and single proteins belonging to the dpp, ras and wg/Wnt signaling pathways (Table 1). Identification of these known regulators of midgut cell death validates the possibility that other proteins relevant to midgut degradation are contained within this dataset.

Functional classification of differentially abundant proteins in dying midguts

To identify differentially abundant proteins, pairwise comparisons between the three stages of midgut cell death (-4 vs +2, -4 vs 0 and 0 vs +2 h RPF) were conducted based on the fold-changes between the developmental stages (log₂ of -4/+2, -4/0 and 0/+2 h RPF) versus p-values (-log₁₀ of Benjamini-Hochberg corrected p-value) for each comparison (Fig. S1). During the -4 h RPF and +2 h RPF developmental stages examined, 232 proteins were differentially expressed (Figure 1D), where 140 proteins increased in abundance and 92 proteins decreased. The abundance of 213 proteins was significantly altered between -4 h and 0 h (129 increased and 83 decreased), and 137 proteins were significantly altered (84 increased and 53 decreased) between 0 h and +2 h developmental stages (Figure 1D).

Subjecting the total number of differentially abundant proteins to hierarchical clustering analysis segregated the proteins into five main clusters (with a few smaller clusters of proteins that sit on their own). This indicates there are groups of proteins that show similar changes in abundance during midgut cell death (Figure 1E; Table S1). To functionally characterize these clusters, proteins from each cluster were subject to gene ontology (GO) term enrichment analysis using the functional annotation clustering tool from the online bioinformatics resource Database for Annotation, Visualization and Integrated Discovery (DAVID) [17,18]. Although there were no significantly enriched terms associated with proteins in cluster 1 (39), 4 (23), and 5 (32), the remaining protein clusters were significantly enriched for multiple GO terms. The most enriched functional group associated with proteins in cluster 2 was the chitin metabolic

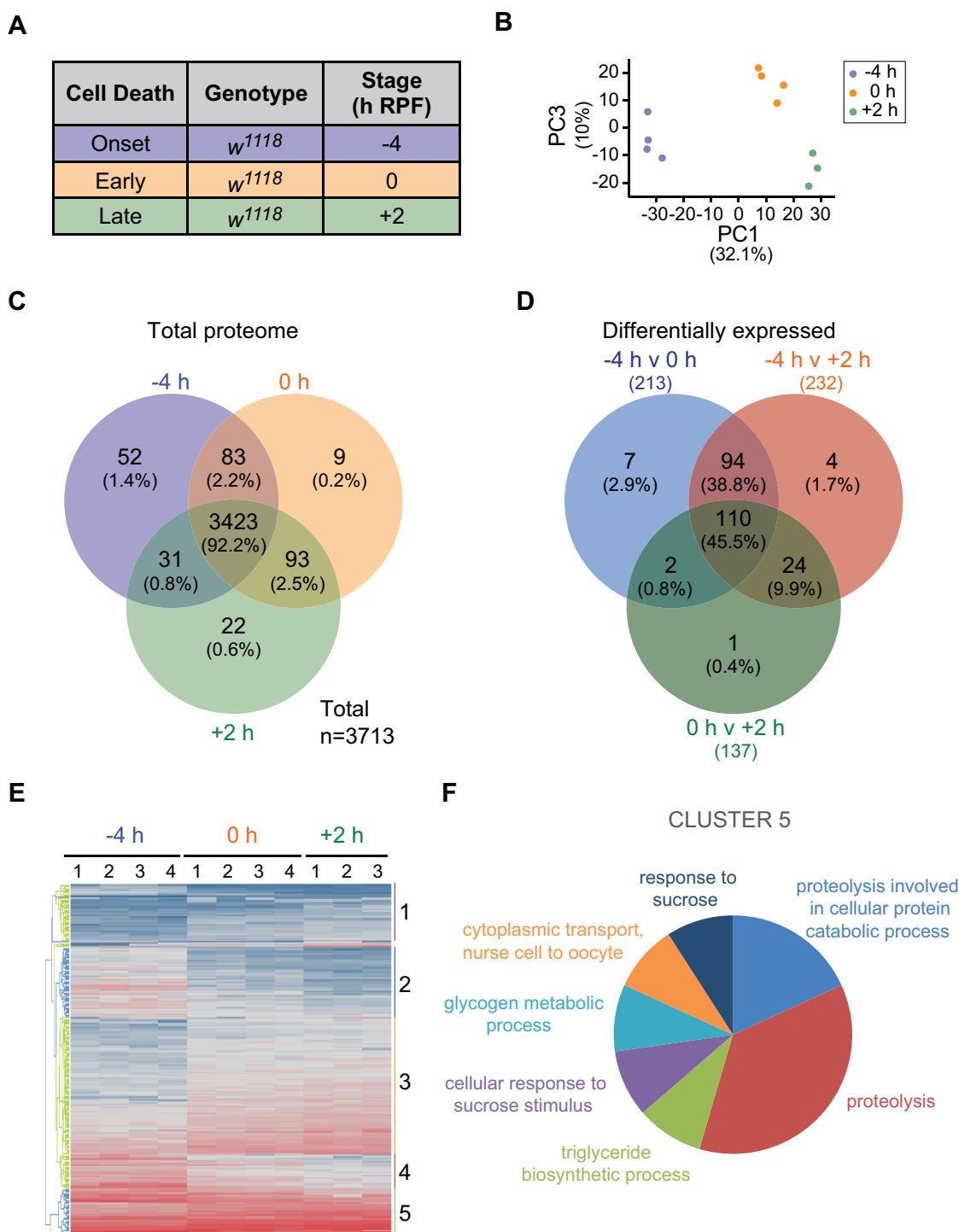


Figure 1. Proteins identified in dying *Drosophila* larval midguts. (A) Experimental design for the identification of proteins present during developmental cell death of *Drosophila* larval midguts using proteomic analysis. Proteins across three stages of midgut degradation (−4, 0 and +2 h RPF) were prepared for proteomic analyses (lysis, digestion using FASP) before nanoflow liquid chromatography-tandem mass spectrometry (LC-MS/MS) and label-free quantitation using MaxQuant. (B) PCA biplot of protein abundance in PC1 and PC3 from four replicates at −4 and 0 h RPF and three replicates from +2 h RPF midgut samples used for analyses (proportion of variance in brackets). Each dot represents a replicate that is color-coded according to the developmental time point (see legend). (C) Three-way Venn diagram summary of total larval midgut proteins at −4 h 0 and +2 h RPF. (D) Three-way Venn diagram summary of unique and overlapping larval midgut proteins that are differentially expressed between the −4 h versus 0 h RPF, 0 h versus +2 h RPF, and the −4 h versus +2 h RPF. (E) Hierarchical clustering of differentially abundant midgut proteins using the \log_2 -transformed average of the sum of normalized peptide intensities for each protein per sample group per replicate. The blue to red color gradient is representative of low to high intensity. Columns represent the replicates (1–4 or 1–3) of each sample group (−4, 0 and +2 h RPF), and rows represent the proteins. A complete list of proteins in each cluster are shown in Supplemental material, **Table S1**. (F) Classification of midgut proteome components gene ontology (Biological Process) analysis of proteins identified as differentially abundant in dying midguts.

process followed by proteolysis, while proteins in cluster 3 were associated with mRNA splicing, via spliceosome, and mitotic nuclear division.

From the analysis of the most differentially changed proteins there was an enrichment in three Kyoto Encyclopedia of Genes and Genomes (KEGG) pathways: lysosome, metabolic

Table 1. Proteins identified that are known to be present in the larval midgut.

Protein group	Symbol	Log ₂ normalized intensity			References
		-4 h RPF	0 h RPF	+2 h RPF	
Autophagy	Atg5	19.49	18.24	19.87	[8,10,42]
	Atg8a	22.19	22.08	22.28	
	Atg9	22.77	21.89	23.25	
	Atg17	20.10	19.46	20.18	
	Atg18a	22.66	22.60	23.19	
	Pi3K59F/Vps34	20.38	20.14	21.30	
PI3K/Tor signaling	Tor	22.02	21.43	21.71	[10,42]
	raptor	20.36	19.49	20.35	
	Pten	17.22	18.07	15.65	
	Tsc1	0.00	18.49	13.48	
Ecdysone response	br	19.84	19.24	20.22	[6,55,56]
	Eip93 F	17.25	0.00	17.51	
	Sox14	18.50	17.32	19.92	
Ubiquitination	Ptp52F	16.67	15.96	17.58	[16,57]
	Ub	25.53	26.59	27.05	
	Uba1 ^a	27.10	26.99	27.59	
	Uba1 ^b	17.95	0.00	18.67	
	TSG101	23.45	23.17	23.68	
Dpp pathway	Med	18.51	19.13	19.16	[15]
Wnt pathway	sgg	24.57	24.72	25.00	[58]
Ras signaling	Ras85D	24.55	24.60	24.84	[42]

^aUniProt entry Q8T0L3 which is 1,191 bp in length. ^bUniProt entry O46111 which is 1,008 bp in length. Symbols are listed according to FlyBase annotation. The log₂ normalized intensities listed are prior to imputation.

pathways and spliceosome components. Of particular interest was a cluster (Cluster 5) that showed Biological Process enrichment for proteolysis and Molecular Function enrichment for proteins that are peptidases, that act on L-amino acid peptides (identifying proteins Cp1, CtsF [Cathepsin F], 26-29-p [26-29kD-proteinase], CG4572, Cndp2 [Cytosolic nonspecific dipeptidase 2], Ppn [Papilin], Jon65Aiv [Jonah 65Aiv]) (Figure 1F; Table S1). Several of these proteins are cathepsins, the lysosomal enzymes that function to break down proteins. Cp1, CtsF and 26-29-p are the *Drosophila* homologs of CTSL, CTSF and CTSK, respectively [19]. With no clear CTSA homolog in *Drosophila*, CG4572 is most similar to mammalian CPVL (carboxypeptidase vitellogenic like) and CTSA. Of these, the proteomics analysis identified a 4-fold increase in the abundance of Cp1 in the dying midgut. The upregulation of Cp1 in the larval midgut suggests that developmentally regulated proteolysis may mediate changes that occur during midgut degradation.

Lysosomes are specialized organelles that function to break down and recycle cellular components from vesicular pathways such as secretory, endocytic, autophagic and phagocytic pathways. The lysosome contains hydrolytic enzymes including cathepsin proteases, which are activated by the acidic pH within the lysosome generated by proton-pumping vacuolar-type H⁺-ATPase (V-ATPase) [20]. An essential final step in autophagy is the fusion between autophagosomes and lysosomes to form autolysosomes. The resulting acidic environment promotes activation of the enzymes required for degradation and recycling of autophagic cargos. Given the importance of the lysosome to autophagy and the identification of several cathepsins or putative cathepsins in the proteomics analysis, we investigated their *in vivo* function in autophagy-dependent midgut degradation.

Cp1 is abundant in the midgut and increases during degradation

The most abundant differentially expressed protein during midgut degradation was Cp1 (Figure 2A; Table S1). Consistent with the proteomics data, Cp1 protein and transcript levels increased during midgut degradation (Figure 2B, C). Analysis of wild-type midgut protein extracts by immunoblotting with Cp1 antibody showed an increase in between -4 h RPF and +2 h RPF (Figure 2B). We observed both the pro and mature forms with the mature form predominant at 0 and +2 h RPF [19,21,22]. Similarly, *Cp1* transcript was detected in midguts at -4 h RPF with increased levels detected during midgut degradation at 0 and +2 h RPF (Figure 2C). Previously, *in situ* hybridization has detected expression of *Cp1* in embryonic and larval midgut [23]. We examined the protein localization of Cp1 in the midgut and found punctate localization, which increased during midgut degradation (Fig. S2). The punctate localization of Cp1 during midgut degradation colocalized with Atg8a puncta (Figure 2D,E). Lysosomal enzyme precursors are transported to the lysosome via the endosomal pathway. To determine the subcellular localization of Cp1 during midgut degradation, we examined double labeling of Cp1 with markers of membrane-bound compartments of the endolysosomal pathway. Cp1 colocalized with the late endosomal and lysosomal marker Lamp1 (Figure 2D, E). Cp1 also partially colocalized with the endosomal marker Rab7, with the early endosomal marker Rab5 and with Rab11 marked recycling endosomes (Figure 2D,E). This is consistent with Cp1 trafficking to the lysosome in midgut cells at the onset of removal, which then accumulates during midgut degradation.

Cp1 is required to maintain normal autophagy levels

Degradation of the midgut involves a large change in midgut size initially due to the contraction of four anterior appendages known as the gastric caeca and an overall reduction in size [7]. During this size reduction, autophagy progressively increases and is strongly detected at +2 h RPF [8,16]. Having established that Cp1 protein levels increase during midgut cell death, we next examined the effect of *Cp1* knockdown using the highly specific midgut driver, *Mex-GAL4*, on midgut degradation. Both Cp1 mRNA and protein levels were significantly reduced following *Cp1* RNAi knockdown (Fig. S3A and S3B). Similarly, the immunostaining of Cp1 was reduced in *Cp1* knockdown midguts (Fig. S3C). We found that *Cp1* knockdown using the GD RNAi line that showed greater transcript reduction, resulted in increased gastric caeca size at -4 h RPF (Figure 3A), while the KK RNAi line was similar to control (Fig. S3D). This size increase was also observed at +2 h RPF but was not seen at 0 h RPF and did not dramatically alter the progression of midgut contraction as the size at +4 h RPF was similar to the control (Fig. S3F and S3G).

To examine the level of autophagy in whole midguts, we monitored mCherry-Atg8a puncta formation. This revealed that *Cp1* knockdown had increased levels of Atg8a puncta at the onset of midgut degradation at -4 h RPF compared to controls (Figure 3B, 3F and S3E). In addition to the increase

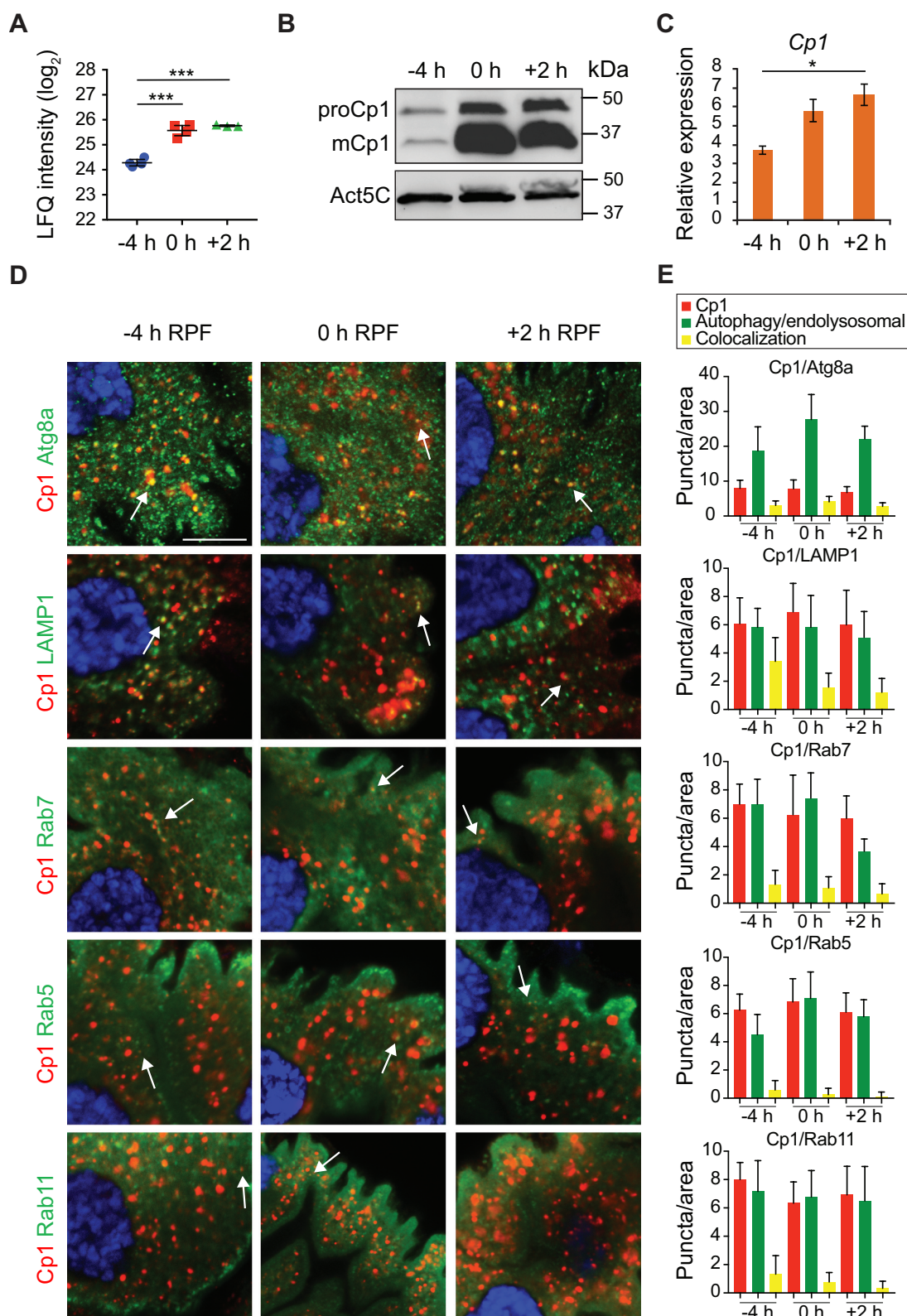


Figure 2. Cp1 localizes to late endosomes and lysosomes in the midgut. (A) LFQ intensity of Cp1 at -4 h RPF, 0 h RPF and $+2$ h RPF as measured by mass spectrometry. Biological replicates for -4 and 0 h RPF ($n = 4$) and 3 for $+2$ h RPF ($n = 3$), error bars \pm SD. *** $p < 0.0001$. (B) Immunoblot analysis of Cp1 with protein lysates from midguts during degradation at -4 h RPF, 0 h RPF and $+2$ h RPF showing increased Cp1 levels in wild-type (w^{1118}) with Act5C (Actin 5 C) as load control. The inactive proform of Cp1 (proCp1) is ~ 40 kDa and the mature form (mCp1) is ~ 35 kDa. (C) The level of *Cp1* transcripts from wild-type (w^{1118}) larval midguts at -4 h RPF, 0 h RPF and $+2$ h RPF were measured by qRT-PCR from total RNA extracts. *RpL32* mRNA was used as the reference gene. Data are from three independent experiments, each containing 10 midguts per group (means \pm SEM). (D) Immunostaining of Cp1 (red) with autophagy marker Atg8a (*Mex-GAL4/+; pGFP-Atg8a/+*) (green) and endolysosomal markers Rab5, Rab7, Rab11 and LAMP1 (*Mex-GAL4/+; UAS-GFP-Rab5/+*, *Mex-GAL4/+; UAS-GFP-Rab7/+*, *Mex-GAL4/+; UAS-Rab11* and *Mex-GAL4/UAS-GFP-LAMP1*) (green). DNA is stained by Hoechst (blue). Scale bar: $10 \mu\text{m}$. (E) Quantification of puncta per area from (D) with Cp1-positive puncta (red), various autophagy/endolysosomal markers (green) and colocalized puncta (yellow) (average puncta/area \pm SD).

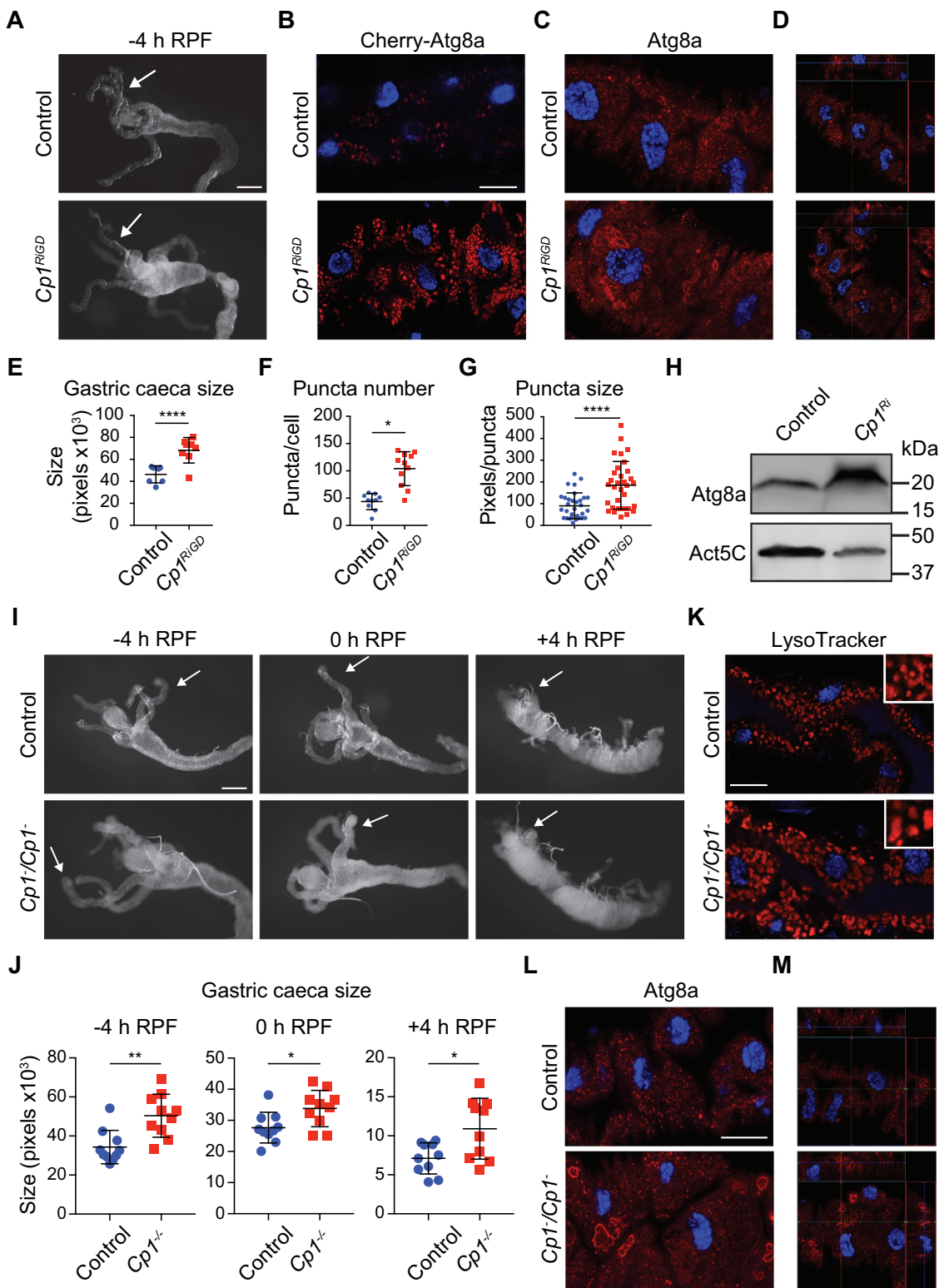


Figure 3. Loss of *Cp1* alters autophagy in the midgut. (A) Morphology from control (*Mex-GAL4/+; pmCherry-Atg8a/+*) and *Cp1^{Ri}* knockdown (*Mex-GAL4/UAS-Cp1 GD RNAi; pmCherry-Atg8a/+*) midguts from -4 h RPF shows larger size gastric caeca (arrows). Scale bar: 200 μ m. (B) The knockdown of *Cp1^{Ri}* has increased mCherry-Atg8a-marked autophagic vesicles (red) in the larval midguts at -4 h RPF compared to controls. DNA is stained by Hoechst (blue). Scale bar: 50 μ m. (C) The Atg8a immunostaining (red) of midguts at -4 h RPF shows that *Cp1^{Ri}* has enlarged Atg8a vesicles compared to controls. DNA is stained by Hoechst (blue). Scale bar: 20 μ m. (D) Orthogonal Projection of Atg8a staining shows abnormal vesicles in the *Cp1^{Ri}*. (E) Quantification of gastric caeca size from (A) (average pixels \pm SD, **** $p < 0.0001$). (F) Quantification of Cherry-Atg8a puncta number from (B) (average \pm SD, * $p = 0.0156$). (G) Quantification of Cherry-Atg8a puncta size from (B) (average \pm SD, **** $p < 0.0001$). (H) Immunoblot analysis of protein lysates from control and *Cp1* knockdown midguts at -4 h RPF shows increased level of Atg8a in *Cp1* knockdown compared to control with Act5C as load control. (I) Morphology from control (*Cp1^{Ri}/+*) and *Cp1⁻/Cp1⁻* midguts from -4, 0 and +4 h RPF shows increased size of midgut and gastric caeca in the *Cp1⁻/Cp1⁻* mutants (arrows). Scale bar: 200 μ m. (J) Quantification of gastric caeca size from (I) (average pixels \pm SD, -4 h RPF ** $p = 0.0018$, 0 h RPF * $p = 0.0202$, +4 h RPF * $p = 0.0133$). (K) LysoTracker Red staining (red) of midguts at -4 h RPF shows that *Cp1⁻/Cp1⁻* has enlarged vesicles compared to controls (*Cp1^{Ri}/+*), inset is enlarged section. DNA is stained by Hoechst (blue). Scale bar: 20 μ m. (L) The Atg8a immunostaining (red) of midguts at -4 h RPF shows that *Cp1⁻/Cp1⁻* has enlarged Atg8a vesicles compared to controls (*Cp1^{Ri}/+*). DNA is stained by Hoechst (blue). Scale bar: 20 μ m. (M) Orthogonal Projection of Atg8a staining shows abnormal vesicles in the *Cp1⁻/Cp1⁻* mutant.

in puncta number, the size of the Atg8a puncta was larger in *Cp1* knockdown compared to the control (Figure 3G). Consistent with the increased Cherry-Atg8a puncta number and size, Atg8a immunostaining revealed the accumulation of abnormal Atg8a-positive structures (Figure 3C,D). The increased Atg8a levels were also detected in immunoblot of *Cp1* knockdown midgut lysates compared to controls (Figure 3H). Interestingly, however, at later stages (0 and +2 h RPF) there was no significant difference in the number of Atg8a puncta (Fig. S3H and S3I). The increase in Atg8a puncta in the *Cp1* knockdown midguts at -4 h RPF suggests that Cp1 activity is required to maintain normal basal levels of autophagy prior to degradation. Surprisingly, while the knockdown of *Cp1* increased autophagy puncta, this did not result in premature size contraction of the midgut (Figure 3) as is seen with *Tor* knockdown, where premature induction of autophagy correlates with premature size reduction [10,24].

We confirmed these results by analyzing a *Cp1* mutant allele (Figure 3I-M) [25]. The morphology of the larval midgut was examined during degradation. This showed a significant increase in size of *Cp1* mutant midgut at -4 h RPF, and while the *Cp1*⁻ mutant midgut contracted during midgut degradation at 0 h and +4 h RPF, it remained larger than the control (Figure 3I,J). The increased midgut size in the *Cp1*⁻ mutant was greater than that observed following *Cp1* knockdown (Figure 3 and S3). This is likely to be due to the level of knockdown of the RNAi lines compared to the stronger mutant allele.

In *Drosophila*, LysoTracker staining can be used as a marker to detect autophagy-associated lysosomal activity in the midgut [10,26]. There was a dramatic increase in the size of the LysoTracker-positive vesicles at -4 h RPF in the *Cp1*⁻ mutant midgut cells (Figure 3K). Similarly, Atg8a immunostaining revealed the accumulation of abnormal Atg8a-positive structures similar to those seen in the *Cp1* knockdown (Figure 3C,D,L,M). This striking phenotype indicates an essential role for Cp1 in biogenesis of autophagic vesicles in the midgut.

Abnormal autophagic vesicles accumulate following *Cp1* knockdown

To further investigate the increased autophagy puncta in *Cp1*-deficient midgut cells, we generated clones in the midgut that give rise to cells knocked down for *Cp1* adjacent to control cells. Interestingly, the *Cp1* knockdown clone cells displayed increased Atg8a puncta size at -4 h RPF compared to the neighboring control cells suggesting a cell-autonomous accumulation of enlarged autophagic vesicles (Figure 4A,B). To further investigate the increase in autophagy puncta size, we undertook ultrastructural analysis, which showed that the *Cp1* knockdown midguts contained abnormal autolysosomal structures (Figure 4C). In the *Cp1* knockdown midgut cells, there were large vesicles containing undigested cytoplasm that were not observed in the control cells (Figure 4C). The morphology of these vesicles

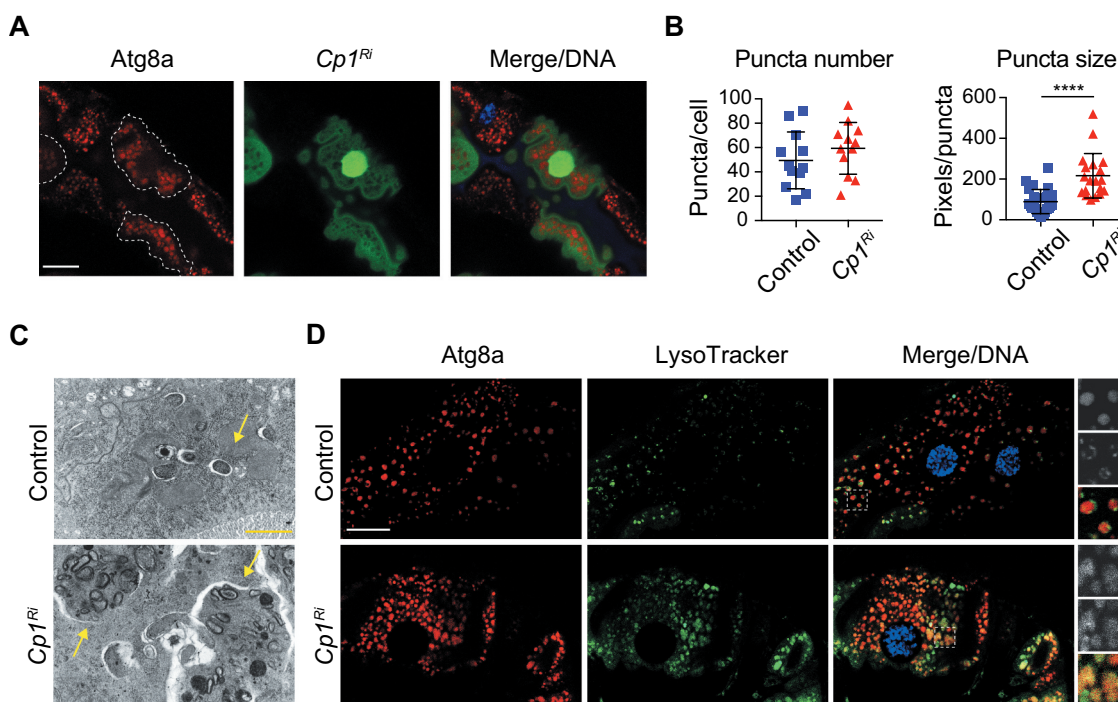


Figure 4. *Cp1* knockdown increases autophagy puncta size and accumulation of abnormal autophagic vesicles. (A) Clone cells of *Cp1* knockdown (*hsFLP*; *pmCherry-Atg8a*^{+/+}; *Act>CD2>GAL4, UAS-nlsGFP/UAS-Cp1*^{RNAi}) marked by GFP (green) have increased mCherry-Atg8a puncta size (red, outlined) compared to the neighboring control cells at -4 h RPF. DNA is stained by Hoechst (blue). Scale bar: 20 μ m. (B) Quantification of puncta number and puncta size from (A) (average pixels/puncta \pm SD, **** $p < 0.0001$). (C) Representative Transmission electron microscopy images from sections of midgut at -4 h RPF. Control cells possess autolysosomal structures (arrows), and *Cp1*^{RNAi} knockdown midgut cells have abnormal autophagic structures. Scale bar: 1 μ m. (D) mCherry-Atg8a puncta (red) and LysoTracker green (green) shows that in the knockdown of *Cp1*^{RNAi} there is increased colocalization in the larval midguts at -4 h RPF compared to controls. The right-hand side images show a higher magnification of the indicated region with mCherry-Atg8a (top), LysoTracker (middle) and merge (bottom). Scale bar: 20 μ m.

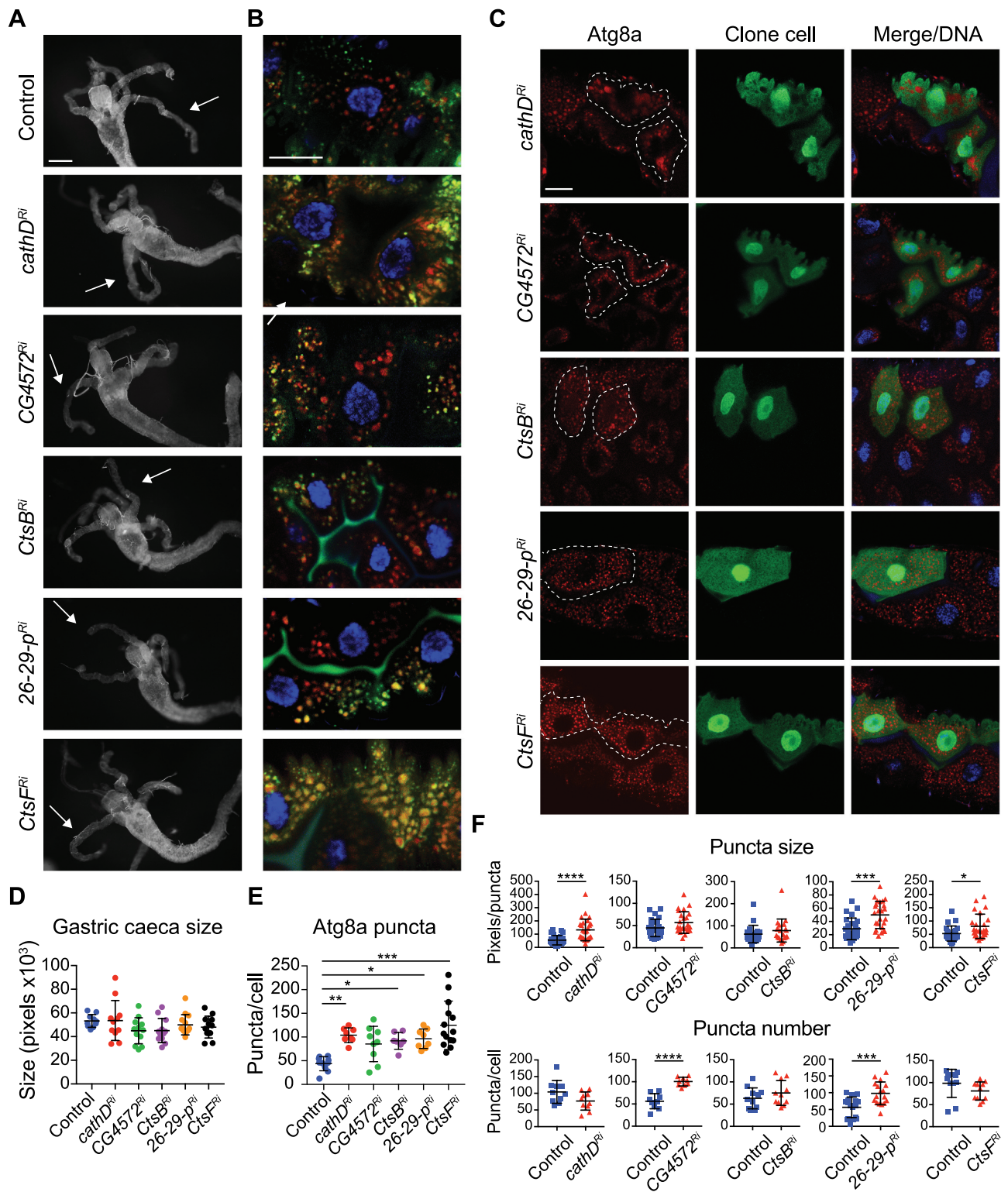


Figure 5. Knockdown of cathepsins alters autophagy but not size reduction of the midgut. (A) Morphology from control (*Mex-GAL4/+; pmCherry-Atg8a/+*) and *Cathepsin* knockdown (*Mex-GAL4/UAS-Cathepsin RNAi; pmCherry-Atg8a/+*) midguts from -4 h RPF shows similar size midgut and gastric caeca (arrows). Scale bar: 200 μ m. (B) Co-staining of mCherry-Atg8a puncta (red) and LysoTracker green (green) in the larval midguts at -4 h RPF. DNA is stained by Hoechst (blue). Scale bar: 20 μ m. (C) Knockdown of cathepsins (*hsFLP; pmCherry-Atg8a/+; Act>CD2> GAL4, UAS-nlsGFP*) in clone cells marked by GFP (green) with mCherry-Atg8a puncta (red, outlined) compared to the neighboring control cells at -4 h RPF. DNA is stained by Hoechst (blue). Scale bar: 20 μ m. (D) Quantification of gastric caeca size from (A) (average pixels \pm SD). (E) Quantification of Cherry-Atg8a puncta from (B) (average \pm SD) (* $p < 0.05$, ** $p = 0.004$, *** $p < 0.0001$). (F) Quantification of puncta number and puncta size from clone and control cells from (C) (average puncta/cell and average pixels/puncta \pm SD, * $p < 0.05$, *** $p < 0.001$, **** $p < 0.0001$).

suggests that they may be autolysosomes that are unable to degrade their contents. Thus, the depletion or mutation of *Cp1* results in the accumulation of enlarged autophagic vesicles.

The degradative activity of cathepsins requires the lysosome to maintain an acidic pH. In *Drosophila* tissues, including fat body and midgut, LysoTracker staining has been used as a marker of autophagy-associated lysosomal

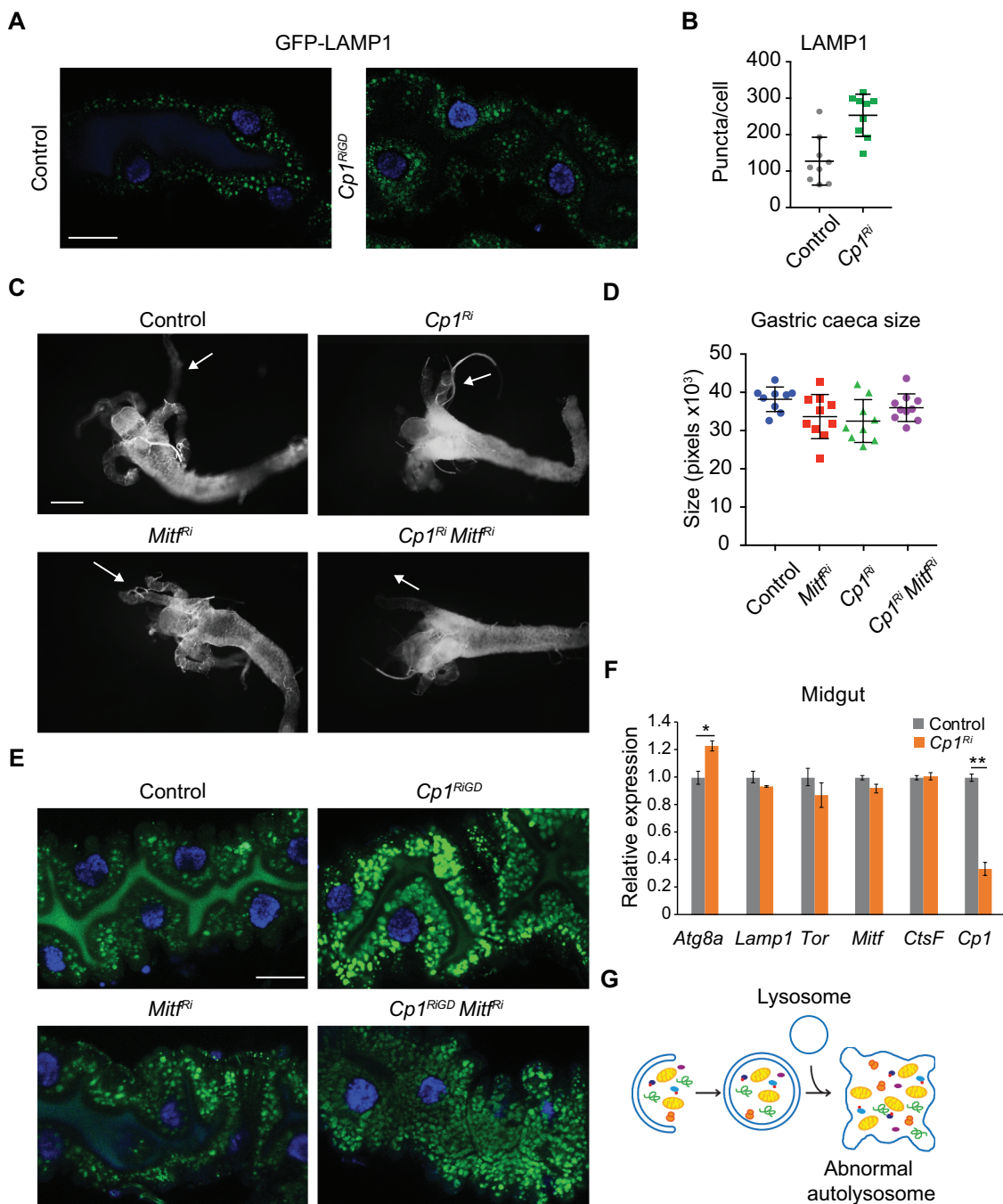


Figure 6. Lysosomal biogenesis is not altered in *Cp1* knockdown. (A) Lysosomes monitored by GFP-LAMP1 puncta (green) shows that knockdown of *Cp1^{Ri}* (*Mex-GAL4*, *UAS-GFP-LAMP1/UAS-Cp1* RNAi) has increased LAMP1-marked vesicles in the larval midguts at -4 h RPF compared to controls (*Mex-GAL4*, *UAS-GFP-LAMP1/+*). DNA is stained by Hoechst (blue). Scale bar: $20 \mu\text{m}$. (B) Quantification of GFP-LAMP1 puncta (average \pm SD). (C) Morphology from control (*Mex-GAL4/+*), *Mitf^{Ri}* knockdown (*Mex-GAL4/+*; *UAS-Mitf* RNAi/+), *Cp1^{Ri}* knockdown (*Mex-GAL4/+*; *UAS-Cp1* RNAi/+), and the double *Mitf^{Ri} Cp1^{Ri}* knockdown midguts from 0 h RPF shows similar size midgut and gastric caeca (arrows). Scale bar: $200 \mu\text{m}$. (D) Quantification of gastric caeca size (average pixels \pm SD). (E) LysoTracker staining (green) of midguts at -4 h RPF shows that *Mitf^{Ri} Cp1^{Ri}* knockdown has similar puncta *Cp1^{Ri}* knockdown compared to control and *Mitf^{Ri}* knockdown. DNA is stained by Hoechst (blue). Scale bar: $20 \mu\text{m}$. (F) The transcript levels of *Atg8a*, *Lamp1*, *Tor*, *Mitf*, *CtsF* and *Cp1* from control (*Mex-GAL4/+*) and *Cp1^{Ri}* (*Mex-GAL4/UAS-Cp1* RNAi) larval midguts (at -4 h RPF) was measured by qRT-PCR from total RNA extracts. *Rpl32* mRNA was used as the reference gene. Data are from three independent experiments, each containing 10 midguts per group (means \pm SEM). (G) Model showing the accumulation of abnormal autolysosomes with undegraded material in the absence of *Cp1*.

activity [10,26]. We assessed acidification of the vesicles using LysoTracker to determine if *Cp1* ablation disrupted lysosomal activity. This staining showed that reduction of *Cp1* levels increased LysoTracker-positive vesicles suggesting functional lysosomes (Figure 4D). This is somewhat unexpected given that cathepsin ablation was predicted to

result in degradation defects and nonfunctional lysosomes. Defective fusion of autophagosomes with lysosomes is likely to lead to an accumulation of autophagosomes and a reduction of autolysosomes. To determine if there is a defect in autophagosomes fusion with lysosomes, the colocalization of Cherry-Atg8a with

LysoTracker was examined. Consistent with increased Atg8a puncta, the *Cp1* knockdown midgut cells also had increased LysoTracker staining (Figure 4D). There was also colocalization of Cherry-Atg8a with LysoTracker, suggesting that in addition to an increase in autophagosomes, *Cp1* knockdown leads to accumulation of autolysosomes.

The identification of LysoTracker-positive vesicles indicates that acidification of autolysosomes and lysosomes can occur in the *Cp1*-depleted midguts. The accumulation of enlarged autolysosomes indicates that autophagosome-lysosome fusion was not impaired in the absence of *Cp1*. Thus, the formation of autophagic vesicles is not compromised in *Cp1*-depleted midguts, and they fuse with lysosomes. However, these abnormal autolysosomes cannot degrade their internal contents despite the fact that their lumen appears to be acidic. The continual fusion of newly formed autophagosomes results in the progressive accumulation of enlarged, dysfunctional autolysosomal structures in *Cp1*-depleted midguts. Hence, initiation of autophagy is normal and the fusion of autophagosomes with lysosomes is not affected in *Cp1* knockdown midguts.

Cathepsin depletion increases autophagy puncta

There are several classes of cathepsins, with the majority being cysteine proteases (CTSB, CTSE, CTSK, CTSL and CTSS). Others include CTSD an aspartic protease and CTSG and CTSA that are serine proteases. Given the identification of additional cathepsins in the proteomics data, we analyzed the cysteine peptidases CtsB (CTSB), 26–29-p (CTSK), CtsF (CTSF); serine-type carboxypeptidase CG4572 (putative CTSA); and aspartic peptidase, cathD (CTSD). These were identified in the proteomics with 26–29-P and CtsF, showing a significant increase in abundance yet did not have an increase in transcript levels (Fig. S4). The additional peptidases identified in the proteomics, Cndp2 and Ppn, showed an increase in protein level with *Ppn* also showing a corresponding increase in transcript level, whereas Jon65Aiv that was expressed at high levels showed a decrease in protein levels (Fig. S4A and S4B) and were not analyzed any further.

Given that several of these cathepsins (or putative cathepsins) were identified in a cluster with *Cp1* we examined if they also had a defect in autophagy. To examine the requirement of these enzymes for ADCD, we systematically knocked down the cathepsin genes in the midgut (Figure 5 and S5). The knockdown of *cathD*, *CG4572*, *CtsB*, 26–29-p of *CtsF* did not affect the size contraction of the larval midgut during degradation at –4 h RPF (Figure 5A,D). Similarly, at all other time points examined from 0 h RPF to the later stage condensed midgut at +4 h RPF, the developmental degradation occurred normally (Fig. S5A and S5B).

Monitoring of autophagic flux following knockdown of the cathepsins in the midgut revealed that *cathD* and *CtsF* ablation led to a significant increase in Atg8a puncta (Figure 5B, E). The knockdown of *CtsB* and 26–29-p also had increased levels of Atg8a puncta at –4 h RPF compared to controls, and while not significant due to the variation in samples there was a trend toward increased Atg8a puncta in *CG4572* knockdown

(Figure 5B,E). To further investigate the increased Atg8a puncta, we generated clones in the midgut that give rise to cells knocked-down for the cathepsins adjacent to control cells. Interestingly, the *cathD*, 26–29-p and *CtsF* knockdown clone cells displayed increased Atg8a puncta size (Figure 5C, F). The dramatically large puncta observed in *cathD* knockdown cells was similar to that of *Cp1* knockdown (Figure 4A, B, 5C,5F). The 26–29-p knockdown clone cells also displayed increased number of Atg8a puncta at –4 h RPF as did *CG4572* knockdown compared to the neighboring control cells (Figure 5C,F). While the puncta size and number in the *CtsB* knockdown clone cells were similar to the control, the *CtsB* knockdown cells had a small but significant increase in cell size compared to the control cells (Figure 5C,F and S5C). While the Atg8a puncta analysis in the whole tissue knockdown showed an increase in Atg8a, the further clonal analysis revealed that this was due to distinct alterations to either puncta size, puncta number (or both) or cell size alterations following the different cathepsin knockdowns. Together, this suggests that the individual cathepsins may have distinct roles in the midgut during ADCD.

Lysosome biogenesis is not altered during midgut degradation

We found that loss of *Cp1* leads to a dramatic increase in the number of autophagic vesicles and lysosomes. These compartments are not defective as they acidify properly, based on LysoTracker staining (Figure 5C). To confirm the effect of *Cp1* knockdown on lysosome numbers, the localization of GFP-LAMP1 fusion protein was examined. In the midgut, lysosomal markers LysoTracker and GFP-LAMP1, show low levels at –4 h RPF of degradation coincident with the increase in autophagy [26]. In the control midgut basal levels of GFP-LAMP1 were observed, whereas *Cp1*-depleted midguts showed an increase in GFP-LAMP1 accumulation (Figure 6A). This is consistent with the increase in LysoTracker-positive vesicles (Figure 4D).

The phenotype resulting from ablation of *Cp1* showing an expansion of autolysosomes and lysosomes may be caused by two processes: an increase in biogenesis regulated by transcription of lysosomal and autophagic genes or a defect in lysosomal degradation. The biogenesis and abundance of lysosomes are controlled by a complex transcriptional program that responds to cellular requirements. In mammalian cells, a genetic program coordinated by the TFEB (transcription factor EB) controls lysosomal biogenesis and function [27]. In *Drosophila*, the single *TFEB* ortholog, *Mitf* (microphthalmia associated transcription factor), is involved in lysosomal metabolism and regulation of the lysosomal-autophagic pathway in the brain and fat body [25,28]. In contrast, oxidative stress-induced autophagy regulated by Cnc (Cap-n-collar), the *Drosophila* homolog of mammalian NFE2L2/NRF2 (nuclear factor, erythroid 2 like 2), occurs independently of *Mitf* [29]. Interestingly, *Mitf* reporter expression is not detected in the larval midgut [25]. However, to determine whether the autophagy-lysosomal phenotypes in *Cp1*-ablated midguts are due to TFEB-mediated biogenesis, we examined the knockdown of *Mitf* in the midgut. We did not observe an overall change in autophagy induction or midgut degradation

following *Mitf* knockdown (Fig. S6A). Furthermore, the knockdown of *Mitf* combined with *Cp1* knockdown had similar midgut morphology as the *Cp1* knockdown alone (Figure 6C,D). The LysoTracker staining showed that the combined *Mitf* and *Cp1* knockdown has similarly enlarged lysosomes as the *Cp1* knockdown alone (Figure 6E). This suggests that *Mitf* is not required for ADCD, and that the *Cp1* ablation phenotype is not dependent on *Mitf*-induced lysosomal biogenesis.

To further confirm this, the transcription of genes associated with increased lysosomes was examined in *Cp1* knockdown midguts (Figure 6F). While *Atg8a* expression was increased, there was no increased expression detected for *Lamp1*, *Tor* or *Mitf*. In addition, there was no increased expression of *CtsF*, suggesting that *Cp1* ablation does not result in compensatory expression of other cysteine cathepsins.

These results suggest that the observed lysosomal expansion following *Cp1* ablation is unlikely to be due to increased lysosomal biogenesis. Therefore, lysosomal expansion may be caused by a degradation defect rather than increased biogenesis and the *Cp1* knockdown impairs lysosomal degradation. Thus, the autophagic phenotype of *Cp1* knockdown is not likely to be due to failures in the initial steps of autophagy induction, autophagosome formation, autophagosome-lysosome fusion, but due to impairment of degradation of their content resulting in an accumulation of abnormal autolysosomes. Together, these findings provide compelling evidence to indicate that cathepsin loss results in the accumulation of autophagosomes and autolysosomes (autophagic vesicles), without interfering with lysosomal acidification or biogenesis (Figure 6G).

Discussion

Using the label-free proteomics approach, we have generated a comprehensive dataset of proteins present in *Drosophila* midguts undergoing ADCD. Several proteins known to be required for autophagy-dependent midgut degradation were present in this dataset. This also identified differentially abundant proteins and revealed that midgut degradation is associated with changes in *Cp1* abundance. Here, we have demonstrated that *Cp1* deficiency leads to an accumulation of aberrant autophagosomes and autolysosomes likely due to impairment of lysosomal degradation.

Autophagic flux can be separated into three main steps: formation of autophagosomes, fusion of autophagosomes with lysosomes, and degradation of autolysosomal contents. Our results indicate that *Cp1* is not required for autophagosome-lysosome fusion or lysosomal acidification. Rather, the function of *Cp1* is important in degradation of the autophagosomal cytoplasmic contents in the autolysosome. It is intriguing that *Cp1* ablation increased autophagosomes under basal conditions. One possible explanation is that the accumulation of aberrant/defective autolysosomes may act as a trigger to induce selective autophagy of the lysosomes in an attempt to remove them, however, this remains to be determined. There was also a large proportion of lysosome and autophagy markers indicating an accumulation of autolysosomes. This raises the question of how lysosome

biogenesis/homeostasis is maintained under conditions where the lysosomes are consumed as autolysosomes.

The increase in autophagy puncta observed in -4 h RPF midguts following *Cp1* knockdown is distinct to that observed by knocking down *Tor*, which increases autophagy but also results in premature midgut size contraction [10,24]. This distinction supports that *Cp1* knockdown causes a block in autophagy flux and suggests that *Cp1* knockdown results in the accumulation of autolysosomes under growth conditions. However, an unexpected finding from this analysis of *Cp1* ablation in the midgut was that *Atg8a* puncta were eventually similar to control at a later time (0 and +2 h RPF) during midgut degradation. This suggests that *Cp1* deficiency results in the accumulation of autolysosomes under growth conditions, yet at later growth-independent stages during ADCD autolysosome maturation can still occur. This is similar to the finding that nutrient starvation alone can regulate autolysosome maturation [30]. In mammalian cells, *Rab7* depletion results in accumulation of autolysosomes only under nutrient-rich conditions that are rapidly cleared following nutrient starvation [30]. Thus, the importance of autolysosome maturation to autophagy flux appears to be evolutionarily conserved.

Our data shows that *Mitf* knockdown does not affect autophagy or midgut degradation and that *Mitf* transcript levels are not altered by *Cp1* knockdown. This suggests that *Mitf* is not essential for ADCD. There may also be a novel tissue-specific regulatory mechanism to coordinate the expression of genes that control autophagy and lysosomal biogenesis associated with midgut degradation. Importantly, the *Cp1* knockdown phenotype is not altered when combined with *Mitf* knockdown, suggesting that the phenotype due to *Cp1* ablation in the midgut is not dependent on *Mitf*-induced lysosomal biogenesis.

During *Drosophila* metamorphosis, the hormonally induced degradation of the larval salivary glands is mediated by autophagy- and apoptotic-dependent cell death [7,31,32]. Proteomics analysis of dying salivary glands also identified *Cp1*, *CathD* and *CG4572* [33]. In addition, several cathepsins (including *CtsB*, *cathD*, *CtsF* and *Cp1*) are differentially expressed during salivary gland cell death [34]. It is possible that cathepsins are also important in salivary gland cell death, but this remains to be explored. Similar to the phenotype of *Cp1* knockdown in the midgut, the knockdown of V-ATPase subunits, that disrupts lysosomal acidification, also leads to accumulation of enlarged, defective autophagic vesicles in the larval fat body [35]. Thus, cathepsins are likely to have more widespread importance in maintenance of autophagy flux.

Our *in vivo* findings in the context of *Drosophila* midguts undergoing autophagy-dependent cell death are consistent with previous studies showing that loss of *CTSL* prevents autolysosomal protein degradation resulting in enlarged and persisting autolysosomes. Over 20 years ago, the morphological analysis of cultured hippocampal slices from rats treated with *CTSB* and *CTSL* inhibitor identified an accumulation of abnormal lysosomes in neurons [36]. More recently, neurons from *ctsb* (cathepsin B) and *ctsl* (cathepsin L) double knock-out mouse brains have been shown to accumulate abnormal vacuolar structures that display an autophagy marker [37,38]. In *ctsl*-deficient mouse embryonic fibroblasts, autophagy

induction by nutrient deprivation or rapamycin treatment lead to the accumulation of large autolysosomes [39]. In this study, we further establish the essential function of Cp1 in autolysosome biogenesis *in vivo*, using the powerful genetic techniques available in *Drosophila*. Our genetic and cellular analyses reveal the importance of Cp1 in the clearance of autolysosomes *in vivo*. Combined with studies in mammals cited above, our findings support an evolutionarily conserved function of Cp1/CTSL in autolysosomal maturation.

In mammals, other cathepsins are also required to maintain normal vesicle homeostasis. For example, *Ctss*-deficient macrophages show an accumulation of mitophagic vesicles [40] and *Ctsd*-deficient neurons accumulate abnormal vesicles resembling autophagosomes [38]. The accumulation of abnormal autophagic vesicles can also result from defects in both transport and maturation. In *Ctse*-deficient macrophages, autophagic flux is perturbed however this is due to impaired fusion of autophagosome to lysosomes [41]. This suggests a distinct role of CTSE upstream of autophagosomal fusion rather than the accumulation of aberrant autolysosomes revealed from our *in vivo* finding with Cp1. Together with our studies, this suggests that the specific function of the individual cathepsins is not redundant and may depend on their unique proteolytic targets.

It is well established that autophagy leads to fusion of autophagosomes and lysosomes forming autolysosomes, whereby autophagosome cargo is degraded. However, how this feeds back to autophagy flux, the fate of the autolysosome (maturation) and the effect on lysosome homeostasis is poorly understood. These results indicate that cathepsins play an important role in the regulation of autophagic flux by maintaining a degradative environment inside the lysosome. Given the contribution of cathepsin dysfunction to numerous diseases, a greater understanding of the role of cathepsins and the lysosome to autophagic flux is essential for further development of potential therapeutic compounds that modulate autophagy.

Materials and methods

Fly stocks

The midgut driver *Mex-GAL4* was obtained from Richard Burke (Monash University, Vic., Australia), pmCherry-Atg8a is described in [42] and pGFP-Atg8a is described in [8]. The following stocks were from the Bloomington *Drosophila* Stock Center (Bloomington, IN, USA): *w¹¹¹⁸*, *UAS-w^{IR}* (28980), *Cp1* mutant (*w^{*}*; *Cp1*[*CC01377*]/*SM6a*) BL 51555, *UAS-26-29-p* (*CG8947*) (*y¹ sc^{*} v¹ sev²¹*; *P* {*TRiP.HMS00675*} *attP2*) BL32887, *CG4572* (*y¹ sc^{*} v¹ sev²¹*; *P* {*TRiP.HMS01325*} *attP2*) BL34337, *Mitf* (*y¹ sc^{*} v¹ sev²¹*; *P* {*TRiP.HMS02712*} *attP2*) BL43998, *UAS-GFP-Rab5* (*w^{*}*; *P*{*UAS-GFP-Rab5*}3) BL43336, *UAS-RFP-Rab7* (*w^{*}*; *P*{*UAS-Rab7.GFP*}3) BL42705, *UAS-Rab11-GFP* (*w^{*}*; *P*{*UAS-Rab11-GFP*}2) BL8506, *UAS-GFP-LAMP1* (*w^{*}*; *P*{*UAS-GFP-LAMP*}2). VDRC RNAi lines: *CtsB* (*CG10992*) (KK) v108315, *CtsF* (*CG12163*) (KK) v107589, *cathD/CyO* (*CG1548*) (KK) v109651, *Cp1*(KK) v110619, *Cp1*(GD) v13959. The control was *w¹¹¹⁸* crossed to *Mex-GAL4*, or relevant driver line. The verification and knockdown quantification of the RNAi lines was determined

by qRT-PCR from late third instar larvae, from a minimum of 3/sample in triplicate. All flies were maintained and crosses performed at 25°C on cornmeal, molasses and yeast medium. Several of the KK RNAi lines may overexpress the *tiptop* (*tio*) gene [43], and we have shown that *tio* overexpression does not alter midgut degradation (data not shown).

Larval staging and midgut morphology analysis

To stage larvae, wandering third instars were raised on standard media supplemented with 0.05% bromophenol blue (Sigma-Aldrich, B6131) and transferred to Petri dish with moist Whatmann paper to monitor for gut clearance as visualized by loss of blue in the gut (−4 h RPF) [44]. For morphological analysis, a minimum of 10 midguts from appropriately staged animals were dissected in 1x phosphate buffered saline (PBS; Sigma-Aldrich, P4417), fixed in 4% formaldehyde (Sigma-Aldrich, 252549) in 1xPBS and imaged using a stereozoom microscope (Olympus, Tokyo, Japan). The size of the gastric caeca was measured from these images using Photoshop (Adobe, San Jose, CA, USA) magnetic lasso tool and the histogram function to determine pixels included in the area as previously described [42].

Live mCherry and LysoTracker imaging

For live imaging of mCherry-Atg8a, a minimum of 10 midguts were dissected from appropriately staged animals in 1xPBS with Hoechst 33342 (2 µg/ml; Invitrogen, H1399) to stain DNA and imaged immediately without fixation using a Zeiss confocal (LSM 700 or 800; Carl Zeiss Microscopy, Jena, Germany). The images were quantitated using ImageJ (Bethesda, MD, USA) to count puncta with a size larger than 2 pixels and represented as the average puncta per cell. For co-staining with LysoTracker, a minimum of 10 midguts were dissected in 1xPBS with 1 µM LysoTracker Red DN99 or LysoTracker Green DND26 (1:1000; Invitrogen Molecular Probes, L7528 and L7526 respectively) and Hoechst 33342. The images were quantified using ImageJ to count puncta with a size larger than 30 pixels and represented as the average puncta per cell.

Puncta size measurement

A randomly selected fixed size area was analyzed using Photoshop magic wand tool with the sample size set as point sample and tolerance set at 50. Individual puncta in each fixed area were selected and the histogram function was used to determine the number of pixels and the average puncta size. Three areas were measured from each image with a total of 10 images examined.

Immunostaining and immunoblotting *Drosophila* midguts

Midguts of the required stages were dissected in 1xPBS and fixed with 4% w:v paraformaldehyde (Sigma-Aldrich, P6148) in 1xPBS at room temperature for 20 min then washed 3 × 5 min in PBTw (PBS + 0.1% Tween 20 [Sigma-Aldrich, P7949]). Midguts were blocked in PBTx (PBS + 0.1% Triton

X-100 [Sigma-Aldrich, T8787]) containing 1% bovine serum albumin heat-shock fraction (Sigma-Aldrich, A7904) at room temperature for 1 h then incubated with rabbit anti-CTSL/MEP (1:200; Abcam, 58991), goat anti-GFP (1:200; Rockford, 600-101-215) or anti-Atg8a (Anti-GABARAP + GABARAPL1 + GABARAPL2; Abcam, 109364) overnight at 4°C. Following 4 × 30 min washes in PBTx, midguts were incubated with anti-rabbit Alexa-FLUOR 555 (1:200; Invitrogen Molecular Probes, A27039) and anti-goat Alexa-FLUOR 488 (1:200; Invitrogen Molecular Probes, A11055), at room temperature for 1 h. Samples were washed 3 × 10 min in blocking buffer, stained with Hoechst 33342 for 1 min, and washed 3 × 10 min in PBTx. Midguts were mounted in 80% glycerol (Sigma-Aldrich, G7893) in 1xPBS and imaged on a Zeiss confocal microscope (LSM 700 or 800).

Protein lysates from appropriately staged dissected midguts were denatured for 5 min at 95°C and separated on Mini-PROTEAN TGX Stain-Free pre-cast gels (Bio-Rad, Hercules, CA, USA) at 110 V for 60 min in SDS-PAGE running buffer (250 mM Tris-base [Sigma-Aldrich, T6066], 192 mM Glycine [Sigma-Aldrich, G7126], 0.06% SDS [Sigma-Aldrich, 74255]) and transferred onto PVDF membrane (Perkin Elmer, NEF1002001PK). The membranes were blocked with 5% w/v skim milk powder (Diploma) in TBS-T (20 mM Tris, 150 mM NaCl pH 7.4 [Sigma-Aldrich, S3014], 0.05% Tween 20) for 1 h at room temperature, before incubation with primary antibody anti-CTSL/MEP (1:500; Abcam, 58991), anti-Atg8a (1:500 Anti-GABARAP + GABARAPL1 + GABARAPL2; Abcam, 109364), or mouse anti-Act5C/ACTB/ β -actin (1:1000; Sigma Aldrich, A1978) overnight at 4°C. Membranes were washed in TBS-T for 4 × 15 min before incubation with secondary antibody (anti-rabbit-horse radish peroxidase (HRP)-conjugated; GE healthcare, GENA934 and anti-mouse-Cy5-conjugated; Invitrogen Molecular Probes, A10524) for 1 h at room temperature. Membranes were then washed in TBS-T for 4 × 15 min, followed by development with Enhanced Chemi-Luminescence (ECL) reagent (GE Healthcare, RPN2236) or SuperSignal West Femto Maximum Sensitivity Substrate (Thermo Fisher Scientific, 34096). The luminescence signals were detected using a Fuji LAS4000 System (GE Healthcare, Waukesha, WI, USA) or Chemidoc MP (Bio-Rad, Hercules, CA, USA).

Confocal microscopy

Confocal images were obtained at room temperature using a Carl Zeiss LSM 700 Axio Observer Z1 confocal microscope with 405 nm (5 mW), 488 nm (10 mW) and 555 (10 mW) and 639 nm (5 mW) lasers using Zen 2011 (Black Edition), version 8.1.5.484 (Carl Zeiss Microscopy, Jena, Germany) or a Carl Zeiss LSM 800 Axio Observer 7 confocal microscope with 405 nm (5 mW), 488 nm (10 mW), 561 nm (10 mW) and 640 nm (5 mW) lasers using Zen 2.3 (Blue Edition) (Carl Zeiss Microscopy, Jena, Germany). *Drosophila* midguts were visualized using the PlanApo 40x/1.0 DIC objective on LSM 700 and PlanApo 40x/1.3 Oil DIC objective on LSM 800. Images captured by Zen software were exported into Photoshop (Adobe, San Jose, CA, USA).

Transmission electron microscopy

Midguts from appropriately staged larvae were dissected in 1xPBS then fixed in 1.25% v/v glutaraldehyde (Electron Microscopy Sciences, 16220), 4% w/v sucrose (Chem Supply, SA030), 4% w/v paraformaldehyde (ProSciTech, C007) in 1xPBS for 30 min at room temperature. Samples were then washed with 4% w/v sucrose in 1xPBS, post-fixed in 1% osmium tetroxide (ProSciTech, EMS19102) for 1 h, dehydrated in ethanol, treated with propylene oxide (ProSciTech, C156-450), and infiltrated for embedding in resin (Procure 812 embedding kit; ProSciTech, C038). Ultrathin sections were cut on grids, stained for 2 min with 4% uranyl acetate (Ajax Chemicals Ltd; 569) in 25% ethanol and 2 min in Reynold's lead citrate (Lead Nitrate; Chem Supply, LA019 and tri Sodium Citrate Dehydrate; Chem Supply SA034) before examination using FEI Tecnai G2 Spirit transmission electron microscope (Adelaide Microscopy; FEI Hillsboro, OR, USA).

Quantitative Real-Time PCR (qRT-PCR)

The level of gene expression was determined by qRT-PCR. Total RNA was isolated from 20 midguts/sample or 3 whole larvae/sample in triplicate for each sample using TRIzol reagent (Invitrogen, 15596026). cDNA was synthesized using High Capacity cDNA Reverse Transcription Kit with random primers (Applied Biosystems, 4368814) using 1 μ g of total RNA. qRT-PCR was performed on a Rotor-Gene Q (Qiagen, Valencia, CA, USA) using KAPA SYBR FAST Universal Kit (Sigma-Aldrich, KK4601) as per the manufacturer's instructions. Reactions were performed in triplicate using three independent biological samples, and the transcript levels were normalized using *RpL32* as the reference gene. Data were analyzed using the Q-Gene software (Qiagen, Valencia, CA, USA) with Standard Curves [45], and samples on the same graph were run simultaneously. Primers used are listed as follows:

RpL32 F 5'-CCAGTCGGATCGATATGCTAA; R 5'-ACGTTGTGCACCAGGAAGCTT
CG4572 F 5'-CTCCTCGCTCTTCGGTTTGT; R 5'-ATAGCCGGCATCGTTCTCTG
CtsB F 5'-TTTGCTGTGTCAGCGCATTG; R 5'-CATCGAAATTGCGACCCACC
cathD F 5'-AATCAAGATGGATGCCGCCT; R 5'-CCGGCAATTGGGGAATGAGA
CtsF F 5'-GAAGGGAAATGAGACCGCCA; R 5'-ACACCGTGGTCGAGGTTTTT
Cp1 F 5'-CGATTTGCTGCACCACGAAT; R 5'-GTGTCCTGATCCTTGACGG
Atg8a F 5'-CATCGGTGATTTGGACAAGA; R 5'-TGCCGTAAACATTCTCATCG
Tor F 5'-CGGTTATCCCGCTCAGTACC; R 5'-GGTGATCATAGTCTGGCGCA
Mitf F 5'-AATATGATTGAGCGAAGGCG; R 5'-AAGATTGTCCCCTTGTTTGG
Lamp1 F 5'-TGCTGCCTGAGGATTTTCCA; R 5'-ACTGCTCAGCATCGAGTGTC

Ppn F 5'-CGCTTATTGTGCTGTCCTGC; R 5'-CAGGGAATCTGCTCTGGGAA

Cndp2 F 5'-TGATAAATGGGCCGAGCGAG; R 5'-GAATAGATCCCCCTTCGCGG

Jon65Aiv F 5'-TACCAGGTGGGACTTTCCT; R 5'-AGTAGACGGTCACGGACTGA

Mass spectrometry analysis

Four biological replicates of 20 midguts each were collected from -4, 0 and +2 h RPF *w¹¹¹⁸* animals. Samples were resuspended in 6 M urea (Sigma-Aldrich, 33247), 100 mM DTT (DL-Dithiothreitol Sigma-Aldrich, D9163) and 100 mM Tris-HCl pH7.0 and subjected to protein digestion using a filter aided sample preparation (FASP) column [46]. Solvent was removed by lyophilization before peptides were resuspended in 3% acetonitrile (ACN; Fisher Chemical, A955-4) and 0.1% formic acid (FA; Merck, 5.33002.0050). Samples were analyzed by nanoflow LC-MS/MS on a nanoAcquity system (Waters, Milford, MA, USA) coupled to a Maxis quadruple Time Of Flight (qTOF) mass spectrometer (Bruker, Bremen, Germany) through a CaptiveSpray ion source with nitrogen source gas doped with acetonitrile (Bruker). Peptide mixtures were separated by reverse-phase chromatography using a 250 mm column with 75 μ m inner diameter (nanoAcquity UPLC 1.7 μ m BEH130 C18) on a 90 min linear gradient from 1% to 35% buffer B (A: Milli-Q water, 3% ACN, 0.1% FA; B: 99.9% ACN, 0.1% FA) at a 400 nl/min constant flow rate. The Maxis qTOF was operated in a data-dependent mode with a 1.5 second cycle time, switching automatically between one full-scan (4 Hz) and subsequent MS/MS scans for the remaining time.

The raw files were analyzed using the MaxQuant software (version 1.5.7.4) [47,48]. The database search was performed using *Drosophila melanogaster* protein sequences obtained from Uniprot including isoforms with strict trypsin specificity allowing up to 2 missed cleavages. The minimum required peptide length was set to 7 amino acids. Carbamidomethylation of cysteine was set as a fixed modification while N-acetylation of protein N-termini and oxidation of methionine were set as variable modifications. During the MaxQuant main search, precursor ion mass error tolerance was set to 0.006 Da and fragment ions were allowed a mass deviation of 40 ppm. PSM and protein identifications were filtered using a target-decoy approach at a false discovery rate (FDR) of 1%.

Further analysis was performed using a custom pipeline developed in R, which utilizes the MaxQuant output files (allPeptides.txt, peptides.txt and evidence.txt.) A feature was defined as the combination of peptide sequence, charge and modification. Features not found in at least half the number of replicates in each group were removed. Proteins identified from hits to the reverse database and proteins with only one unique peptide were also removed. To correct for injection volume variability, feature intensities were normalized by converting to base 2 logarithms and then multiplying each value by the ratio of maximum median intensity of all replicates over median replicate intensity. Features assigned to the same protein differ in the range of intensity due to their chemico-physical properties and charge state. To further correct these differences, each intensity value was multiplied by the ratio of the maximum of

the median intensities of all features for a protein over the median intensity of the feature. Missing values were imputed using a random normal distribution of values with the mean set at mean of the real distribution of values minus 1.8 SD, and an SD of 0.3 times the SD of the distribution of the measured intensities. The probability of differential expression between pairwise groups was calculated using a Mann Whitney U-test excluding any non-unique sequences and any features with modifications other than oxidation and carbamidomethylation. Probability values were corrected for multiple testing using Benjamini-Hochberg method.

A principal component analysis (PCA) using the log2 intensity values of all peptides detected in the -4, 0 and +2 h RPF midgut samples was performed to examine the variability between the replicates for each sample. This separated the replicates into distinct groups according to their developmental stage except for one of the +2 h RPF samples (Fig. S1). This replicate was excluded from further analysis, and additional PCA revealed the replicates clustered more closely following the removal of the sample (Figure 1B). Therefore, the proteomes of midguts from different developmental stages were generated using four biological replicates for both -4 and 0 h RPF samples, and three biological replicates for the +2 h RPF sample.

The mass spectrometry proteomics data have been deposited to the ProteomeXchange Consortium via the PRIDE [49] partner repository with the dataset identifier PXD016675.

Bioinformatics

The obtained Universal Protein Knowledgebase (UniProt v2.16; <http://www.uniprot.org>) [50] accession numbers were processed through Database for Annotation, Visualization & Integrated Discovery (DAVID) bioinformatics resources v.6.7 (<https://david.ncifcrf.gov/>) [17,18], Kyoto Encyclopedia of Genes and Genomes (KEGG) pathway maps (<http://www.genome.jp/kegg>) [51,52] and Protein ANalysis THrough Evolutionary Relationships (PANTHER) classification system (<http://pantherdb.org>) [53,54].

Statistical analysis of data

Student's t-test, two-tailed equal variance was used for statistical analysis to compare two groups and data are expressed as mean \pm standard deviation (SD) or mean \pm standard error of the mean (SEM), as appropriate. $P < 0.05$ was considered significant. For multiple analyses, an ordinary one-way analysis of variance (ANOVA) with Tukey's multiple comparisons test was performed using Prism (GraphPad Software) and data are expressed as mean \pm SD.

Acknowledgments

This work was supported by the National Health and Medical Research Council (NHMRC) of Australia Project Grant (1124490), and an Australian Research Council (ARC) Discovery Grant (DP170100623). SK was supported by a NHMRC Senior Principal Research Fellowship (1103006). SN was supported by a Research Training Program scholarship. We thank the Australian *Drosophila* Research Support Facility (Monash University, Vic., Australia), Vienna *Drosophila* Resource Center, and Bloomington *Drosophila* Stock Center for *Drosophila* stocks. We thank the TRIP at Harvard Medical

School (NIH/NIGMS R01-GM084947) for providing transgenic RNAi fly stocks. We thank Ruth Williams at Adelaide Microscopy (Frome Rd, The University of Adelaide, SA, Australia) for assistance with transmission electron microscopy sample preparation and microscopy.

Disclosure statement

The authors declare no conflict of interest regarding the publication of this paper.

Funding

This work was supported by the Australian Research Council [DP170100623]; National Health and Medical Research Council [1103006]; National Health and Medical Research Council [1124490].

ORCID

Jarrod J. Sandow  <http://orcid.org/0000-0001-5684-8236>
 Sonia Dayan  <http://orcid.org/0000-0002-5616-7542>
 Xin Jiang  <http://orcid.org/0000-0003-0991-1436>
 Jantina A. Manning  <http://orcid.org/0000-0001-9142-6135>
 Sharad Kumar  <http://orcid.org/0000-0001-7126-9814>
 Donna Denton  <http://orcid.org/0000-0002-6271-3183>

References

- [1] Kutscher LM, Shaham S. Non-apoptotic cell death in animal development. *Cell Death Differ.* 2017;24:1326–1336.
- [2] Fuchs Y, Steller H. Live to die another way: modes of programmed cell death and the signals emanating from dying cells. *Nat Rev Mol Cell Biol.* 2015;16:329–344.
- [3] Yuan J, Kroemer G. Alternative cell death mechanisms in development and beyond. *Genes Dev.* 2010;24:2592–2602.
- [4] Galluzzi L, Vitale I, Aaronson SA, et al. Molecular mechanisms of cell death: recommendations of the nomenclature committee on cell death 2018. *Cell Death Differ.* 2018;25:486–541.
- [5] Denton D, Kumar S. Autophagy-dependent cell death. *Cell Death Differ.* 2019;26:605–616.
- [6] Lee CY, Cooksey BA, Baehrecke EH. Steroid regulation of midgut cell death during *Drosophila* development. *Dev Biol.* 2002;250:101–111.
- [7] Jiang C, Baehrecke EH, Thummel CS. Steroid regulated programmed cell death during *Drosophila* metamorphosis. *Development.* 1997;124:4673–4683.
- [8] Denton D, Shrivage B, Simin R, et al. Autophagy, not apoptosis, is essential for midgut cell death in *Drosophila*. *Curr Biol.* 2009;19:1741–1746.
- [9] Denton D, Shrivage B, Simin R, et al. Larval midgut destruction in *Drosophila*: not dependent on caspases but suppressed by the loss of autophagy. *Autophagy.* 2010;6:163–165.
- [10] Xu T, Nicolson S, Denton D, et al. Distinct requirements of autophagy-related genes in programmed cell death. *Cell Death Differ.* 2015;22:1792–1802.
- [11] Stoka V, Turk V, Turk B. Lysosomal cathepsins and their regulation in aging and neurodegeneration. *Ageing Res Rev.* 2016;32:22–37.
- [12] Patel S, Homaei A, El-Seedi HR, et al. Cathepsins: proteases that are vital for survival but can also be fatal. *Biomed Pharmacother.* 2018;105:526–532.
- [13] Shen HM, Mizushima N. At the end of the autophagic road: an emerging understanding of lysosomal functions in autophagy. *Trends Biochem Sci.* 2014;39:61–71.
- [14] Karch J, Schips TG, Maliken BD, et al. Autophagic cell death is dependent on lysosomal membrane permeability through Bax and Bak. *Elife.* 2017;6:e30543.
- [15] Denton D, Xu T, Dayan S, et al. Dpp regulates autophagy-dependent midgut removal and signals to block ecdysone production. *Cell Death Differ.* 2019;26:763–778.
- [16] Chang T-K, Shrivage BV, Hayes SD, et al. Uba1 functions in Atg7- and Atg3-independent autophagy. *Nat Cell Biol.* 2013;15:1067–1078.
- [17] Huang da W, Sherman BT, Lempicki RA. Systematic and integrative analysis of large gene lists using DAVID bioinformatics resources. *Nat Protoc.* 2009;4:44–57.
- [18] Huang da W, Sherman BT, Lempicki RA. Bioinformatics enrichment tools: paths toward the comprehensive functional analysis of large gene lists. *Nucleic Acids Res.* 2009;37:1–13.
- [19] Kocks C, Maehr R, Overkleeft HS, et al. Functional proteomics of the active cysteine protease content in *Drosophila* S2 cells. *Mol Cell Proteomics.* 2003;2:1188–1197.
- [20] Perera RM, Zoncu R. The lysosome as a regulatory hub. *Annu Rev Cell Dev Biol.* 2016;32:223–253.
- [21] Hasanagic M, van Meel E, Luan S, et al. The lysosomal enzyme receptor protein (LERP) is not essential, but is implicated in lysosomal function in *Drosophila melanogaster*. *Biol Open.* 2015;4:1316–1325.
- [22] Kowalewski-Nimmerfall E, Schahs P, Maresch D, et al. *Drosophila melanogaster* cellular repressor of E1A-stimulated genes is a lysosomal protein essential for fly development. *Biochim Biophys Acta.* 2014;1843:2900–2912.
- [23] Matsumoto I, Watanabe H, Abe K, et al. A putative digestive cysteine proteinase from *Drosophila melanogaster* is predominantly expressed in the embryonic and larval midgut. *Eur J Biochem.* 1995;227:582–587.
- [24] Denton D, Xu T, Dayan S, et al. Crosstalk between Dpp and Tor signaling coordinates autophagy-dependent midgut degradation. *Cell Death Dis.* 2019;10:111.
- [25] Zhang T, Zhou Q, Ogmundsdottir MH, et al. Mitf is a master regulator of the v-ATPase, forming a control module for cellular homeostasis with v-ATPase and TORC1. *J Cell Sci.* 2015;128:2938–2950.
- [26] Xu T, Kumar S, Denton D. Characterization of Autophagic Responses in *Drosophila melanogaster*. *Methods Enzymol.* 2017;588:445–465.
- [27] Sardiello M, Palmieri M, Di Ronza A, et al. A gene network regulating lysosomal biogenesis and function. *Science.* 2009;325:473–477.
- [28] Bouche V, Espinosa AP, Leone L, et al. *Drosophila* Mitf regulates the V-ATPase and the lysosomal-autophagic pathway. *Autophagy.* 2016;12:484–498.
- [29] Jain A, Rusten TE, Katheder N, et al. p62/sequestosome-1, autophagy-related gene 8, and autophagy in *Drosophila* are regulated by nuclear factor erythroid 2-related factor 2 (NRF2), independent of transcription factor TFEB. *J Biol Chem.* 2015;290:14945–14962.
- [30] Kuchitsu Y, Homma Y, Fujita N, et al. Rab7 knockout unveils regulated autolysosome maturation induced by glutamine starvation. *J Cell Sci.* 2018;131:jcs215442.
- [31] Lee CY, Baehrecke EH. Steroid regulation of autophagic programmed cell death during development. *Development.* 2001;128:1443–1455.
- [32] Berry DL, Baehrecke EH. Growth arrest and autophagy are required for salivary gland cell degradation in *Drosophila*. *Cell.* 2007;131:1137–1148.
- [33] McPhee CK, Balgley BM, Nelson C, et al. Identification of factors that function in *Drosophila* salivary gland cell death during development using proteomics. *Cell Death Differ.* 2013;20:218–225.
- [34] Gorski SM, Chittaranjan S, Pleasance ED, et al. A SAGE approach to discovery of genes involved in autophagic cell death. *Curr Biol.* 2003;13:358–363.
- [35] Mauvezin C, Nagy P, Juhasz G, et al. Autophagosome-lysosome fusion is independent of V-ATPase-mediated acidification. *Nat Commun.* 2015;6:7007.
- [36] Bednarski E, Ribak CE, Lynch G. Suppression of cathepsins B and L causes a proliferation of lysosomes and the formation of mega-neurites in hippocampus. *J Neurosci.* 1997;17:4006–4021.

- [37] Felbor U, Kessler B, Mothes W, et al. Neuronal loss and brain atrophy in mice lacking cathepsins B and L. *Proc Natl Acad Sci U S A*. 2002;99:7883–8.
- [38] Koike M, Shibata M, Waguri S, et al. Participation of autophagy in storage of lysosomes in neurons from mouse models of neuronal ceroid-lipofuscinoses (Batten disease). *Am J Pathol*. 2005;167:1713–1728.
- [39] Dennemarker J, Lohmuller T, Muller S, et al. Impaired turnover of autophagolysosomes in cathepsin L deficiency. *Biol Chem*. 2010;391:913–922.
- [40] Pan L, Li Y, Jia L, et al. Cathepsin S deficiency results in abnormal accumulation of autophagosomes in macrophages and enhances Ang II-induced cardiac inflammation. *PLoS One*. 2012;7:e35315.
- [41] Tsukuba T, Yanagawa M, Kadowaki T, et al. Cathepsin E deficiency impairs autophagic proteolysis in macrophages. *PLoS One*. 2013;8:e82415.
- [42] Denton D, Chang TK, Nicolson S, et al. Relationship between growth arrest and autophagy in midgut programmed cell death in *Drosophila*. *Cell Death Differ*. 2012;19:1299–1307.
- [43] Vissers JH, Manning SA, Kulkarni A, et al. A *Drosophila* RNAi library modulates Hippo pathway-dependent tissue growth. *Nat Commun*. 2016;7:10368.
- [44] Denton D, Mills K, Kumar S. Methods and protocols for studying cell death in *Drosophila*. *Methods Enzymol*. 2008;446:17–37.
- [45] Muller PY, Janovjak H, Miserez AR, et al. Processing of gene expression data generated by quantitative real-time RT-PCR. *Biotechniques*. 2002;32:1372–1379.
- [46] Wisniewski JR, Zougman A, Nagaraj N, et al. Universal sample preparation method for proteome analysis. *Nat Methods*. 2009;6:359–362.
- [47] Cox J, Mann M. MaxQuant enables high peptide identification rates, individualized p.p.b.-range mass accuracies and proteome-wide protein quantification. *Nat Biotechnol*. 2008;26:1367–1372.
- [48] Cox J, Neuhauser N, Michalski A, et al. Andromeda: a peptide search engine integrated into the MaxQuant environment. *J Proteome Res*. 2011;10:1794–1805.
- [49] Perez-Riverol Y, Csordas A, Bai J, et al. The PRIDE database and related tools and resources in 2019: improving support for quantification data. *Nucleic Acids Res*. 2019;47:D442–D50.
- [50] UniProt C. UniProt: a hub for protein information. *Nucleic Acids Res*. 2015;43:D204–12.
- [51] Kanehisa M, Goto S. KEGG: kyoto encyclopedia of genes and genomes. *Nucleic Acids Res*. 2000;28:27–30.
- [52] Kanehisa M, Goto S, Sato Y, et al. Data, information, knowledge and principle: back to metabolism in KEGG. *Nucleic Acids Res*. 2014;42:D199–205.
- [53] Mi H, Muruganujan A, Casagrande JT, et al. Large-scale gene function analysis with the PANTHER classification system. *Nat Protoc*. 2013;8:1551–1566.
- [54] Mi H, Muruganujan A, Thomas PD. PANTHER in 2013: modeling the evolution of gene function, and other gene attributes, in the context of phylogenetic trees. *Nucleic Acids Res*. 2013;41:D377–86.
- [55] Chittaranjan S, McConechy M, Hou YC, et al. Steroid hormone control of cell death and cell survival: molecular insights using RNAi. *PLoS Genet*. 2009;5:e1000379.
- [56] Santhanam A, Liang SY, Chen DY, et al. Midgut-enriched receptor protein tyrosine phosphatase PTP52F is required for *Drosophila* development during larva-pupa transition. *Febs J*. 2013;280:476–488.
- [57] Anding AL, Wang C, Chang TK, et al. Vps13D encodes a ubiquitin-binding protein that is required for the regulation of mitochondrial size and clearance. *Curr Biol*. 2018;28:287–95 e6.
- [58] Xu T, Denton D, Kumar S. Hedgehog and Wingless signaling are not essential for autophagy dependent cell death. *Biochem Pharmacol*. 2019;162:3–13.